Research Papers

Impact of swift heavy ion-induced point defects on nanoscale thermal transport in ZnO

Azat Abdullaev [a,b,*], Kairolla Sekerbayev [a,b], Ruslan Rymzhanov [c,d], Vladimir Skuratov [c,e,f], Jacques O Connell [g], Bekdaulet Shukirgaliyev [h,i,j], Artem Kozlovskiy [k], Yanwei Wang [b,l], Zhandos Utegulov [a,*]

[a] Department of Physics, School of Sciences and Humanities, Nazarbayev University, Astana 010000, Kazakhstan
[b] Laboratory of Computational Materials Science, Center for Energy and Advanced Materials Science, National Laboratory Astana, Astana 010000, Kazakhstan
[c] Joint Institute for Nuclear Research, Dubna 141980, Moscow Region, Russia
[d] The Institute of Nuclear Physics, Ibragimov St. 1, 050032 Almaty, Kazakhstan
[e] Dubna State University, Dubna 141980, Moscow Region, Russia
[f] National Research Nuclear University MEPhI, Moscow 115409, Russia
[g] Centre for HRTEM, Nelson Mandela University, Port Elizabeth, 6001, South Africa
[h] Energetic Cosmos Laboratory, Nazarbayev University, Astana 010000, Kazakhstan
[i] Department of Computation and Data Science, Astana IT University, Astana 010000, Kazakhstan
[j] Faculty of Physics and Technology, Al-Farabi Kazakh National University, Almaty 050040, Kazakhstan
[k] Engineering Profile Laboratory, L.N. Gumilyov Eurasian National University, Astana, 010008, Kazakhstan
[l] Department of Chemical & Materials Engineering, School of Engineering and Digital Sciences, Nazarbayev University, Astana 010000, Kazakhstan

ABSTRACT

Near-surface nanoscale thermal conductivity (k) variation of ion-irradiated single-crystalline ZnO was studied by time-domain thermoreflectance. ZnO was irradiated by 710 MeV Bi swift heavy ions (SHI) in the 10^{10}–10^{13} ion/cm^2 fluence range to investigate the progression *of radiation damage both from single ion impacts and ion path overlapping regimes*. Structural characterization using X-ray diffraction, Raman spectroscopy, and transmission electron microscopy indicated *the absence of amorphization*. The degradation in k *was attributed primarily due to phonon scattering on *point defects*. The results of measured k were used to validate several models including the semi-analytical Klemens-Callaway model, and a novel hybrid modeling approach based on the Monte-Carlo code TREKIS coupled with molecular dynamics simulations which captures the *effects of single ion and ion path overlapping regimes*, respectively. The findings promote a novel approach to developing radiation-controlled thermally functional materials.

1. Introduction

Heat transport is one of the primary phenomena present in almost all energy systems, and significant efforts have been devoted to pushing the lower [1] and upper [2] limits of materials' thermal conductivity (k) and to control the interface thermal boundary conductance (G) between a set of dissimilar materials [3]. Traditionally, control of thermal transport at the nanoscale is achieved via nano-structuring such as creating multi-layers and superlattices [4,5] that are usually aimed at suppressing G by through interfacial diffusive scattering of phonons or enhance it by ballistic transport of phonons. On the other hand, ion implantation and SHI irradiation have been shown to be versatile and efficient methods of generating defects to control material properties, including k [6–8]. Recent studies have shown that ion-induced defects can both suppress and enhance k, owing to recrystallization in single crystalline [9] and amorphous structures [10].

Irradiation with swift heavy ions (SHIs) has recently attracted significant attention as a promising technique for materials nano-engineering [11–13]. SHIs are ions with a mass ranging from 6 to 239 atomic mass units and energies in the hundreds of MeV. During the ion-matter interaction, SHIs excite the electronic subsystem along the ion path, and the subsequent relaxation of electronic excitations results in the formation of nanoscale structures [12]. For certain materials, they can be in the form of cylindrical ion tracks with a typical diameter of

---

* Corresponding authors.
E-mail addresses: azat.abdullaev@nu.edu.kz (A. Abdullaev), zhutegulov@nu.edu.kz (Z. Utegulov).

several nanometer or near-surface defects such as nano-hillocks [14,15]. However, it is still not clear to what extent thermal transport can be controlled in SHI-irradiated structures and how exactly heat conductivity is affected by the radiation-induced near-surface structural variations.

In our recent works using laser-based thermoreflectance methods, we were able to spatially resolve and isolate the thermal conductivities of nanometer and micrometer thickness sub-surface damaged layers of various SHI irradiated insulators [16]. It was found that SHIs can induce disorder in the form of point defects, color centers, and ion tracks. Interestingly, in some materials, they can also lead to subsurface amorphization [16–18]. Moreover, our studies suggested that the crystal structure, ionic bonding strength, and crystal complexity have a strong correlation with the heat conducting behavior of irradiated insulating solids. For example, materials with a larger degree of ionicity and less complex crystal structures are more resistant to track formation, making them more efficient in recrystallization, which therefore leads to recovery of their k to their pristine values at certain ion penetration depths. In addition, we demonstrated that ion-induced nanoscale tracks can lead to anisotropy in thermal transport [19], which opens an avenue for SHI based defect engineering of thermally functional materials.

Fig. 1 shows the degradation in k for various SHI-irradiated insulating single *metal oxide and alkali halide* crystals, among which *ZnO exhibits the highest radiation resistance*. Studies have shown that ZnO can retain its crystallinity even at extreme radiation doses [20]. The main defects caused by ion irradiation are vacancies and interstitials [21]. ZnO is highly resistant to the formation of ion tracks and therefore exhibits a very high threshold electronic stopping power for the creation of visible tracks. This is due to the rapid recrystallization of the melt after SHI-induced thermal spike [22], which is related to the intrinsically high k of ZnO. Several prior studies suggest that highly heat-conductive materials are unlikely to form latent tracks due to efficient heat dissipation and recrystallization [23,24]. The inelastic thermal spike model

has proven successful in predicting track diameters in some dielectrics and semiconductors [25]. In this model, k is one of the critical thermophysical properties determining the material response to irradiation. There is thus a fundamental interest in the evolution of k upon SHI irradiation. Depending on the ion fluence, two different regimes may be distinguished: *single ion (non-overlapping)* and *ion path overlapping regimes.* Both have significant importance in studying the mechanisms of track formation and amorphization of materials [13,25], and it is therefore important to study how thermal transport is affected in these two regimes.

Wide bandgap semiconducting ZnO is also considered as a material for thermoelectric applications due to its relatively low cost, excellent electrical conductivity, and stability at high temperatures [26], and thus the suppression of k is highly desirable. Several approaches have been proposed to enhance the thermoelectric power factor by decreasing the lattice heat transport via nanostructuring [27,28] or by imposing strain to the lattice [29]. Given these considerations, SHI irradiation might also be utilized as an alternative approach to control both thermal and electrical transport properties.

In our prior studies, we used a semi-analytical phonon-mediated Klemens-Callaway kinetic theory to model k in irradiated structures. However, this model is based on fitting specific parameters to experimental data and cannot accurately represents the realistic impact of SHI damage on k. In this study, we present a hybrid modeling approach based on the Monte-Carlo code TREKIS (Time-Resolved Electron Kinetics in SHI Irradiated Solids) coupled with molecular dynamics (MD) simulations to model the impact of SHI irradiation on nano-scale heat propagation in zinc oxide. The simulated structure is used to directly calculate k in the subsurface ion-damaged region. The obtained numerical results are then validated by X-ray diffraction (XRD), Raman spectroscopy, and transmission electron microscopy (TEM). We believe that this research has a far-reaching potential in the further development of advanced laser metrology combined with multi-scale modeling for the assessment of structural defects. It also lays the foundation for further research into radiation-tuned thermally functional materials.

2. Materials and methods

2.1. Materials

High-purity [0001] oriented single crystalline ZnO samples with a wurtzite structure were acquired from MTI Corporation. The investigated samples were $(5 \times 5 \times 0.5)$ mm^3 parallelepipeds polished on the side exposed to SHI irradiation. Irradiation was performed at 60 °C with 710 MeV Bi ions to fluences in the range of 10^{10} - 10^{13} ion/cm^2, using the U-400 FLNR JINR cyclotron facility in Dubna, Russia. The irradiation fluences were selected to cover both single (isolated) impacts and overlapping areas of radiation damage. Ion fluence homogeneity better than 95 % on the irradiated surface was achieved using beam scanning in the horizontal and vertical directions. The ion beam was aligned parallel to the [0001] direction (perpendicular to (0001) planes (c-planes)). For clarity, throughout the manuscript, we refer to the properties parallel to the c-planes of ZnO as "in-plane" and those perpendicular to these planes as "out-of-plane".

Fig. 2a shows the sample geometry for thermal transport measurements (see Section 2.3) and calculated energy loss profile in the irradiated samples. Both the ionization energy loss (S_e) and vacancy profiles along the ion projection range were simulated using the Stopping and Range of Ions in Matter (SRIM 2013) code in full cascade mode [30]. The results are shown in Fig. 2b. The density of ZnO was taken as 5.68 g/cm^3, and the displacement energy for both Zn and O was taken as 50 eV. The heat penetration depth was around 1 μm, while the damage peak was at 24 μm, therefore the probed thermal region was characterized by the maximum ionization losses.
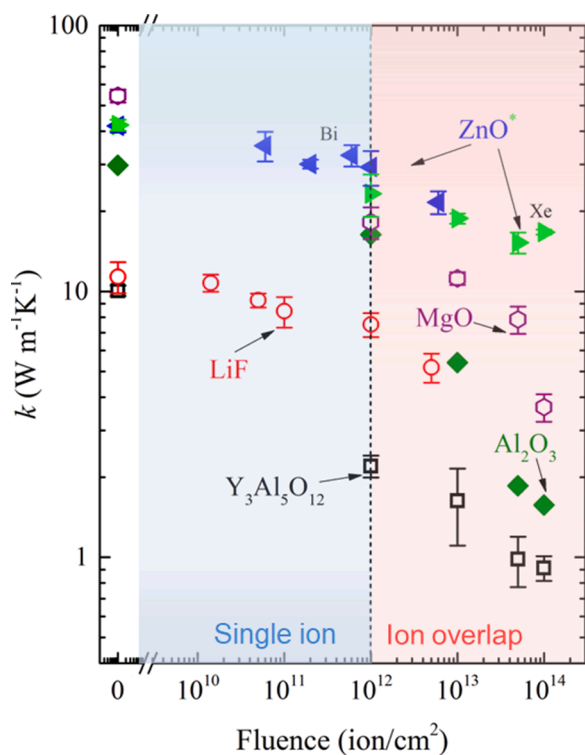

Fig. 1. Thermal conductivity, k, vs ion fluence for materials irradiated with various SHIs: LiF (Bi 710 MeV, [18]), Al$_2$O$_3$ (Xe 167 MeV, [17]), Y$_3$Al$_5$O$_{12}$ (Xe 167 MeV, [16]), MgO (Xe 167 MeV, [16]), ZnO (Xe 167 MeV, [16]) and (Bi 710 MeV, [this work]).
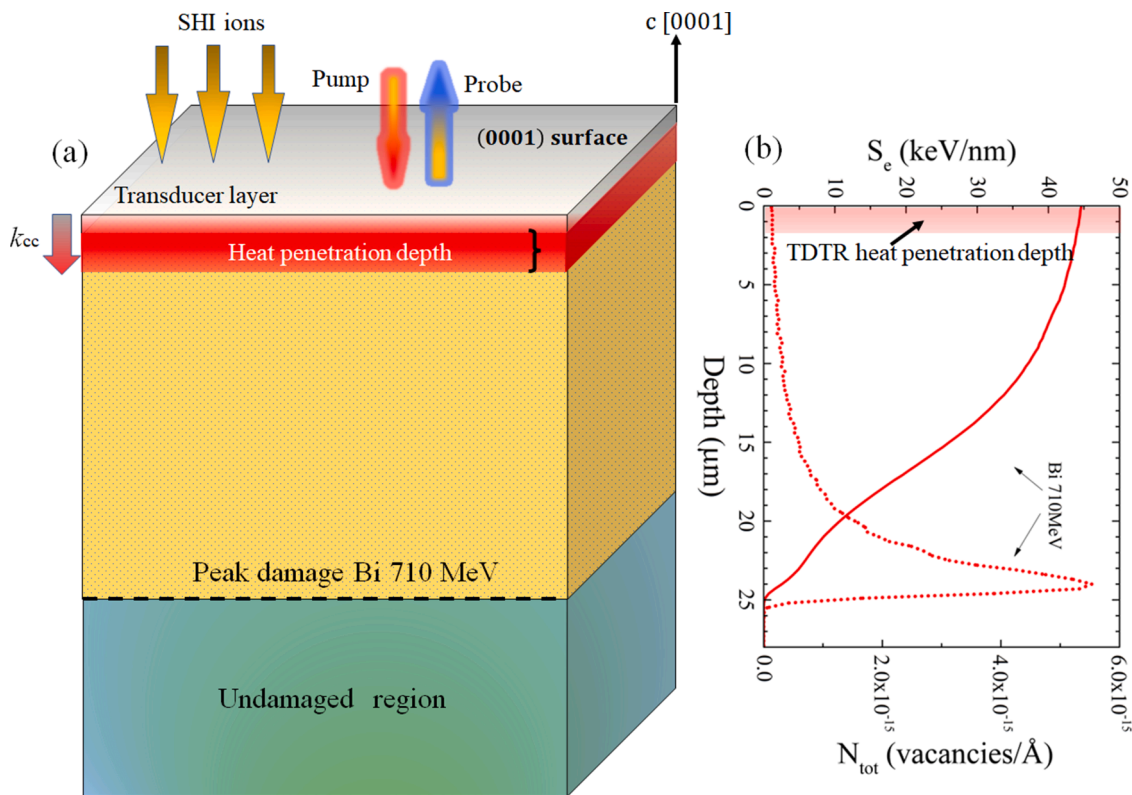
Fig. 2. (a) Schematic view of the SHI irradiated ZnO structure with deposited Al heat transducing layer for thermal measurement (see Section 2.3 below). The direction of the cross-plane thermal conductivity (k_{cc}) and SHI irradiation are along the [0001] direction. The black dashed line denotes peak damage imparted by Bi ions. (b) Ionization energy loss (solid line) and vacancy production profile (dotted lines) in ZnO as a function of projected depth for 710 MeV Bi irradiation. The bottom axis (N_{tot}) shows the corresponding total estimated number of radiation-induced vacancies.

2.2. Structural characterization

For the characterization of SHI-driven structural evolution, the XRD technique was employed using a D8 ADVANCE ECO (Bruker, Germany) powder diffractometer. The single crystal diffraction patterns were recorded in the Bragg-Brentano geometry in the angular range of $2\theta=35–75°$. Prior to taking X-ray diffractograms, specimens were positioned for azimuthal alignment of the c-planes. Defect characterization was performed using a Nanofinder SP Raman microscope (Sol Instruments, Belarus) with 1800 grooves/mm grating and 532 nm single longitudinal mode excitation laser (Torus, Laser Quantum, USA) in backscattering geometry. The incident laser beam was focused onto the sample surface in a spot with a diameter of ~ 2 μm using a 40x microscope objective. The laser power incident on the samples was kept below 10 mW to prevent local heating while maintaining a high signal-to-noise ratio for the measured spectral peaks. The surface roughness of pristine and irradiated samples was characterized by atomic force microscopy (AFM).

Transmission electron microscopy (TEM) analyses were conducted at the center for HRTEM at Nelson Mandela University (South Africa). The samples were imaged in a JEOL ARM-200F TEM operating at 200 kV. All TEM specimens were prepared by FIB using an FEI Helios NanoLab 650. Cross-sectional lamellae were extracted from the bulk irradiated material using the standard FIB lift-out technique. Final polishing of the lamellae was performed at 2 keV Ga beam energy to minimize FIB-induced specimen damage.

2.3. Thermal transport measurements

Thermal characterization was conducted using the well-established femtosecond laser-based time-domain thermoreflectance (TDTR) technique [31], the details of which have been detailed elsewhere [17,18].

Briefly, the emitted laser beam was divided into pump and probe beams. The pump beam was modulated at a 9.8 MHz by an electro-optic modulator to thermally excite the samples while the probe beam was optically scan-delayed by a motorized delay stage. Both light beams were focused onto the sample surface with $1/e^2$ diameter ~10.5 μm. The heat penetration depth is given by $D_{th} = \sqrt{k/\pi C f}$, where C is the volumetric specific heat and f is the pump beam modulation rate, which was varied to control the heat diffusion length in the material. Because the heat penetration depth was negligible compared to the diameter of the focused heating pump laser beam in the TDTR setup, the thermal measurements were sensitive only to cross-plane conductivity as shown in Fig. 2a.

Prior to the thermal probing, pristine and irradiated samples were coated by ~90 nm thick DC magnetron sputtered Al films, serving as metal thermal transducers heating the underlying samples under examination. The thickness of the Al layer was measured using picosecond acoustics. A model based on heat diffusion across a double (Al/ZnO) layer was used to extract the k values of the samples under study by fitting a time-delayed signal of the ratio of in-phase to out-of-phase voltage ($–V_{in}/V_{out}$) [32] as shown in the supplementary material. The material properties, such as density and specific heat, are detailed in Table S1 of the supplementary material, while the thermal conductivity of Al was measured using a reference sample. Two unknown parameters were simultaneously fitted, namely the effective thermal conductivity of the subsurface-damaged region affected by electronic stopping as shown in Fig. 2b, and the interface thermal conductance across the Al/ZnO interface. The measurement errors and uncertainties related to the transducer film thickness were taken into account, and the details are explained elsewhere [17].

2.4. Modelling

2.4.1. Simulation of ion-driven structural damage

The SHI damage was modeled by a hybrid simulation technique combining TREKIS and MD [33–35]. In this integrated approach, TRE-KIS [33–35] was used to predict the radial distribution of energy transferred into the crystal lattice which was then inserted as initial parameters into a classical MD model using the Large-scale Atom-ic/Molecular Massively Parallel Simulator (LAMMPS) code [36]. This approach was previously successfully applied to different non-metals [33,37], including ZnO [37].

TREKIS simulates the dynamics in the ZnO lattice within the first 100 fs following an SHI impact. The simulations used Barkas model for SHI charge [38] in a wurtzite ZnO lattice having a density of 5.68 g/cm^3 and a longitudinal sound velocity of 5850 m/s. A total of 1000 Monte-Carlo iterations were performed for each type of ion.

Utilizing the LAMMPS MD code, the structural relaxation following the impact-induced excitation was studied on a longer time scale ranging from 100 fs to 150 ps [36]. For single ion damage simulations, a ZnO supercell with dimensions of 20.1 × 20.2 × 9.9 nm^3 containing 339 264 atoms was used with periodic boundary conditions applied along all three spatial dimensions. Radial track energy was used to calculate the initial velocities of atoms in cylindrical layers along the [0001] direction of ZnO assuming a Gaussian distribution of kinetic energy in each layer. A microcanonical statistical NVE ensemble (constant number of atoms N, volume V, and total energy E) was applied to internal atoms. Atoms at the boundaries of the supercell along the X- and Y-directions were cooled down by a Berendsen thermostat [39] to an ambient temperature of 300 K. A total relaxation time of 150 ps was found to be sufficient for cooling the atoms down to ambient temperature.

For two sequential incident ions, a damaged ZnO supercell with dimensions 40.3 × 20.2 × 9.9 nm^3 containing 678,528 atoms was considered. The radial distance between the sequential ion paths was varied from 1 to 7 nm.

The resulting damaged ZnO lattices were visualized with OVITO software [40]. Initially, four different Zn-O interatomic potentials (IAP) were considered in our MD simulations, namely Tersoff [41], ReaxFF [42], PCRIM [43] and Buckingham-Coulomb [44] potentials. However, the Tersoff potential yielded an extremely low pristine k value, while the ReaxFF potential was computationally too expensive to determine k. The Buckingham-Coulomb and PCRIM potentials showed similar results. However, PCRIM resulted in better agreement of the predicted results with experimental values. Therefore, we have subsequently employed the PCRIM [45,46] IAP for the rest of the study.

2.4.2. Calculation of lattice k

The lattice k was modeled by three computational methods, as described below. Firstly, equilibrium molecular dynamics (EMD) with the Green-Kubo formalism relates the heat current autocorrelation function (HCACF) to k via [47,48]:

$$k_x = \frac{V}{k_B T^2} \int_0^t \langle J_x(t) J_x(0) \rangle d\tau, \tag{1}$$

where V is the volume of the simulation cell, k_B is the Boltzmann constant, T is the system absolute temperature and t is the correlation time. The heat flux J is defined as:

$$J = \frac{1}{V}\left[\sum_i e_i v_i + \frac{1}{2}\sum_{i<j}\left(F_{ij}\cdot(v_i+v_j)\right)r_{ij}\right], \tag{2}$$

where e_i is the total energy, r_i is the position, and v_i is the velocity of the ith atom. F_i is the force applied to the ith atom.

The EMD method was employed on a 3.9 × 3.9 × 4.1 nm^3 supercell containing 5376 atoms. Before performing the Green-Kubo integration

the supercell was equilibrated for 250 ps with the isobaric-isothermal ensemble (NPT) at 300 K and ambient pressure with the subsequent microcanonical ensemble (NVE) held at 300 K for 250 ps. With a 2 fs time step and 100 ps correlation time, a total accumulation duration of 8 ns was achieved. In EMD simulations the above-mentioned PCRIM IAP was employed. Long-range Coulombic interactions were calculated in the reciprocal $\overrightarrow{K}$-space with a particle-particle-particle-mesh (PPPM) solver [49,50] and with 10^{-6} relative accuracy of estimating the inter-atomic forces. To calculate k for ion-damaged ZnO crystals, the atomic structure was simulated by TREKIS coupled with MD.

The second numerical method for calculating k was based on solving the Boltzmann transport equation using the relaxation time approximation (BTE-RTA) by ALAMODE software [51] coupled with LAMMPS. The lattice k tensor $\kappa_{ph}^{\mu\nu}(T)$ was estimated within RTA as:

$$k_{ph}^{\mu\nu}(T) = \frac{1}{VN_q}\sum_{q,j} c_{qj}(T)v_{qj}^\mu v_{qj}^\nu \tau_{qj}(T), \tag{3}$$

where V is the unit cell volume, $c_{qj} = \hbar\omega_{qj}\partial n_{qj}/\partial T$, v_{qj} is group velocity and $\tau_{qj}(T)$ is the phonon lifetime. Interatomic force constants were obtained from LAMMPS using the MD PCRIM IAP with the supercell containing 64 atoms. Thermodynamic functions including the occupation function, heat capacity, and mean square displacements of atoms were determined using the classical formulae to be consistent with MD simulations in the $\overrightarrow{K}$-space 15 × 15 × 15.

The third numerical approach to calculate k was based on the semi-analytical Klemens-Callaway approximation [52]:

$$k = \frac{1}{3}\int_0^{\frac{\theta_D}{T}} \tau(x)v^2 C(x)dx, \tag{4}$$

where $C(x)$ is the frequency dependent specific heat capacity, $\tau(x)$ is the total phonon relaxation time, θ_D is the Debye temperature, $x = \frac{\hbar\omega}{k_B T}$ is a reduced frequency variable, $\hbar$ is the reduced Planck's constant, ω is the phonon angular frequency and v is the group velocity of phonon heat carriers. The details of this semi-analytical model applied to different materials including Xe ion irradiated ZnO is given in [16,17]. In brief, the degradation in k due to SHI induced damage was captured by phonon scattering via point defects and expressed through a scattering cross section $\Gamma_{irr} = c_{irr}S^2$, where c_{irr} is the average defect density across the probing depth and S^2 is the phonon point defect scattering cross-section defined as $S^2 = (\Delta M/M)^2$. ΔM is the mass difference due to the introduced defects, and M is the atomic mass of host atoms (oxygen). A direct impact model [16,17] was used to determine the $c_{irr} = c_{sat}[1 - \exp(-\sigma\Phi)]$, with Φ being the ion fluence, while c_{sat} and σ were used as free parameters representing the maximum defect concentration and damage cross-section, respectively.

3. Results and discussion

3.1. Structural characterization

The measured XRD patterns indicate that *ZnO preserves its crystallinity even at high ion fluences as shown* in Fig. 3a. The two main observed diffraction peaks at 34.2 and 72.5° were attributed to c-plane 0002 and 0004 reflections, respectively. Both peak intensities decayed with an increase in ion fluence. There was also a shift in both peaks toward lower angles with increasing fluence indicating an expansion of the lattice perpendicular to the c-planes and thus accumulation of compressive stresses. The shift was more pronounced for the 0004 peak as it should be for the higher order reflection. SHI radiation induced swelling is a commonly observed phenomenon and has been reported for several materials for example Al$_2$O$_3$ and ZrO$_2$:Y$_2$O$_3$ [53–56]. Both peaks exhibited slight broadening with increasing fluence. Again, this effect
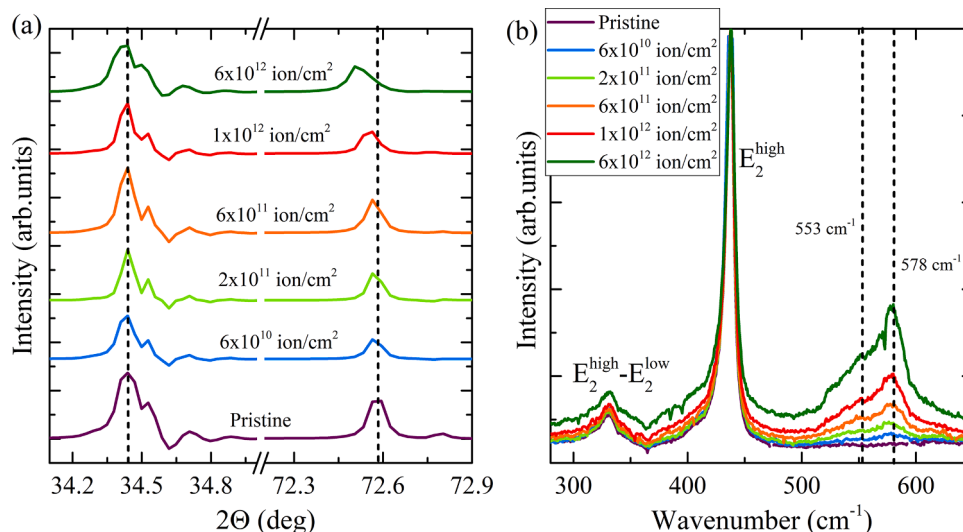
Fig. 3. (a) 2θ XRD pattern and (b) Raman spectra of pristine and irradiated ZnO samples.

was more pronounced for the 0004 peak. This peak broadening is indicative of increased strain in the crystal due to ion induced defects. Due to the specimen geometry, only the *c*-planes were accessible for X-ray diffraction measurement. However, based on consistent reports in the literature it seems reasonable to also expect an increase in the length of the crystal *a*-axis due to irradiation. A more thorough analysis of the XRD data can be found in Table S2 of the supplementary material.

The results of Raman measurements are shown in Fig. 3b. The three main vibrational optical phonon mode peaks observed at 330 cm^{-1}, 436 cm^{-1} and 575 cm^{-1} are characteristic of the wurtzite zinc oxide structure. The highest intensity peak at 436 cm^{-1} is a high frequency E$_2$ (high) mode attributed to the vibration of the nonpolar bonds of O and Zn sub-lattices, and it is an indicator of the purity of the host ZnO crystal structure. The Raman peak at 330 cm^{-1} is an E$_2$ (high)-E$_2$ (low) mode assigned to a multiphonon scattering process [57]. Bi ion irradiation did not cause any significant changes to these two peaks apart from a small variation in intensity. The main difference was seen between 500 cm^{-1} and 600 cm^{-1} with two split peaks at 553 and 578 cm^{-1}, assigned to E$_1$ (LO) and A$_1$ (LO) mode, respectively. These phonon modes are related to intrinsic defects such as zinc interstitials or oxygen vacancies [57–59] present in the as-received unirradiated samples. Both peaks increased gradually in intensity and got broader with ion fluence. This spectral behaviour is consistent with that observed in other SHI irradiated ZnO crystals [58,59] indicating an increase in point defect concentration with fluence.

Fig. 4 shows a cross sectional bright field TEM image of unirradiated ZnO. At the bottom of the image the Al transducer layer can be seen. Image contrast is quite flat over the surface of the ZnO apart from a stronger diffracting region at the bottom left where the foil was slightly bent. Faint "dark spot" contrast is visible uniformly distributed over the specimen surface due to low level FIB induced specimen damage. ZnO is extremely sensitive to ion induced damage in the FIB but the low intensity and uniform distribution of these fain spots made them easily discernable from the much more pronounced Bi induced defects visible in later images.

Fig. 5a shows a bright field TEM image of the 5×10^{11} ion/cm^2 irradiated ZnO. Irradiation direction was from the bottom right as indicated by the arrows. Image contrast is dominated by strain contrast aligned with the ion direction. Defects produced along the ion tracks caused a local lattice distortion that leads to variations in the local diffraction condition. The image in Fig. 5b was recorded at higher magnification in an underfocused condition. Bright streaks are visible just below the irradiated surface from where material was ejected into surface hillocks leaving behind under dense or hollow track cores. The
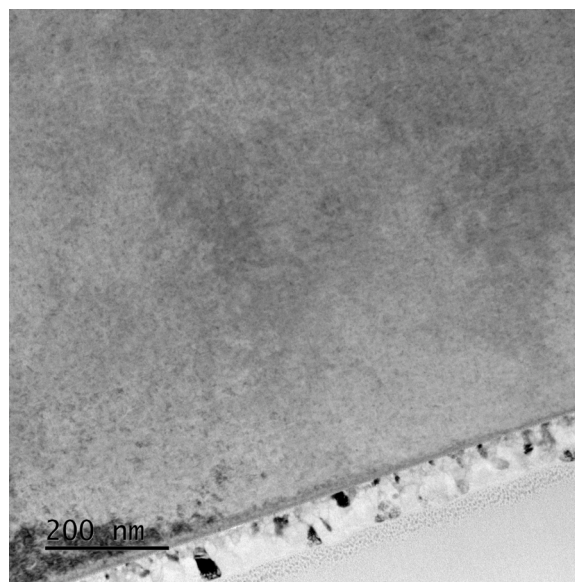

Fig. 4. Cross sectional bright-field TEM image of unirradiated ZnO showing uniform contrast across the ZnO foil.

specimen surface appears rather rough due to Ga beam induced sputtering while depositing a protective carbon layer during FIB lamella preparation as this specimen was prepared for TEM prior to depositing the Al transducer. This damage was limited to about 20–30 nm below the surface as indicated by the dashed line. Deeper into the material, several bright dotted lines are visible along the ion direction and represent small, aligned clusters of vacancies.

Fig. 6a shows the 6×10^{10} ion/cm^2 irradiated specimen after quasi-static annealing at 600 °C in air for 60 min. Strain contrast was largely reduced, and the individual features were much smaller and no longer elongated along the ion direction. Raman results suggested that most of the optically active point defects have recombined after annealing (disappearance of 578 cm^{-1} mode) and while TEM is not sensitive to isolated point defects, it is clear that some defect clusters remained, which were able to locally strain the crystal. The two techniques together suggest that the defect population evolved from a combination of isolated point defects and clusters to mostly clusters (with some level of strain reduction) after annealing. The higher magnification,
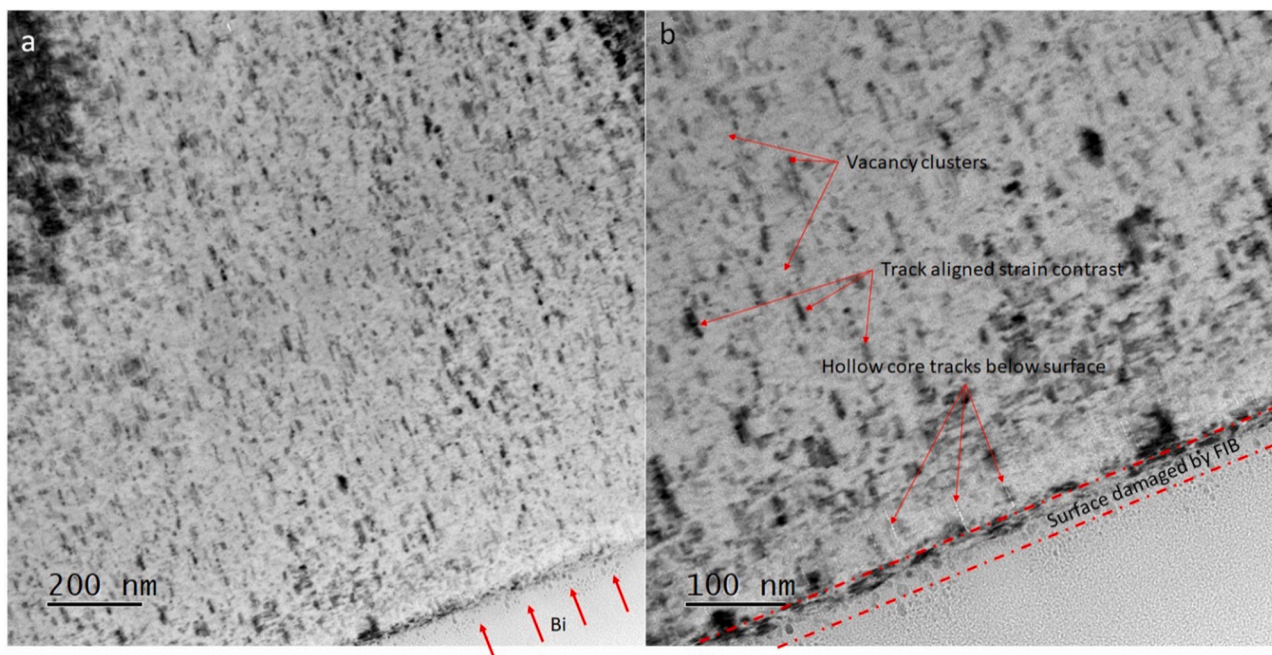
Fig. 5. (a) Cross-sectional bright-field TEM image of 5×10^{11} ion/cm^2 irradiated ZnO. (b) Higher magnification, underfocussed view showing under dense tracks near the surface as well as deeper in the crystal.

underfocused inset shows that the hollow core tracks were still present below the surface. No void clusters were visible beyond these surface related tracks as in the 5×10^{11} ion/cm^2 irradiated specimen. Fig. 6b shows a bright field image of the 6×10^{12} ion/cm^2 irradiated specimen after annealing at the same condition as the low dose sample. Several dislocations were clearly visible after annealing due to defect migration and coalescence. The underfocused inset shows a high density of hollow tracks remaining near the surface down to about 200 nm as well as several void trains deeper below the surface as indicated by the arrows. These features were stable under annealing and increased in size and density with increasing irradiation fluence. They also did not seem to produce much strain contrast suggesting that the surrounding material was not significantly stressed by the presence of these defects.

3.2. Thermal conductivity measurements

Prior to conducting TDTR, an AFM surface morphology analysis was carried out as TDTR measurements are sensitive to surface roughness. The surface roughness of the unirradiated, as-received sample was ≤ 3 nm. Irradiated ZnO samples had slightly elevated roughness in the range of 3–8 nm. The overall ion-induced roughness were acceptable and did not affect the accuracy of TDTR results. AFM images can be found in the supplementary material.

Fig. 7a shows TDTR results for Bi irradiated ZnO. The dashed line corresponds to the measured $k_{cc} \sim 42$ W $m^{-1} K^{-1}$ for pristine ZnO along the [0001] direction which is in agreement with prior literature values [29,60]. Overall, k_{cc} gradually decreased with ion dose, dropping to half of its initial value at 6×10^{12} ion/cm^2. Based on the Raman, XRD and TEM analysis, we conclude that the main reason for such a drop was the formation of mostly radiation-induced O vacancies and Zn interstitials, together with small voids/vacancy clusters in the bulk and hollow tracks near the surface.

Recovery of the thermal conductivity to the level of pristine ZnO was detected after quasi-static annealing of low ion dose irradiated ZnO at 600 °C in air for 60 min due to effective annihilation of radiation induced point defects. Recovery in the higher dose specimens was not complete, and the conductivity values saturated at ~ 35 W $m^{-1} K^{-1}$. However, the Raman spectrum of the 6×10^{12} ion/cm^2 irradiated

sample showed that the broad peak at 578 cm^{-1} mostly disappeared after annealing (inset of Fig. 7a). This behavior can be attributed to the migration of point defects and the subsequent formation of complex defect structures such as vacancy clusters [57] and dislocations [61] as observed in TEM above. Earlier studies [57] have shown that oxygen vacancies produced in ZnO by P^+ implantation become mobile at elevated temperatures and significant agglomeration into vacancy clusters was observed above 400 °C with almost no detectable optically active vacancies remaining after annealing between 600 and 700 °C. It is worth mentioning that the porosity near the irradiated surface observed by TEM could also affect the interface thermal conductance (ITC) between the Al transducer layer and the ZnO surface as shown in Fig. S3 of the supplementary material. However, the ITC did not change significantly after annealing (and from TEM results these structures appear unaffected by annealing) and were thus not a major factor in the observed recovery in the thermal conductivity after annealing.

Our TDTR measurements were performed at 9.8 MHz, which corresponded to a *heat penetration depth of ~ 620 nm*. TEM analysis reveals considerable porosity in the first ~200 nm below the irradiated surface, which should adversely affect the k_{cc} value. To verify this point, we performed frequency modulated TDTR measurements on the 6×10^{12} ion/cm^2 irradiated sample before and after annealing. The pump beam was modulated at lower frequencies in order to increase the heat penetration depth. From Fig. 7b it is evident that the thermal conductivity of the annealed sample increased slightly as the modulation frequency was reduced from 9.8 MHz to 6.8 MHz. We also observed a slight drop in the thermal conductivity at 1.3 MHz but a similar drop was also observed for the unannealed sample. This was likely because at this modulation rate our measurement sensitivity was rather low, leading to a lower signal-to-noise ratio and corresponding drop of the measured thermal conductivity. A recovery in conductivity between 9.8 MHz and 6.8 MHz was not seen for the unannealed specimen suggesting that the effect of the surface porosity was relatively insignificant compared to that of scattered point defects and lattice strain. This again suggests that the crystalline quality was reasonably high in the annealed specimens despite the obvious porosity.
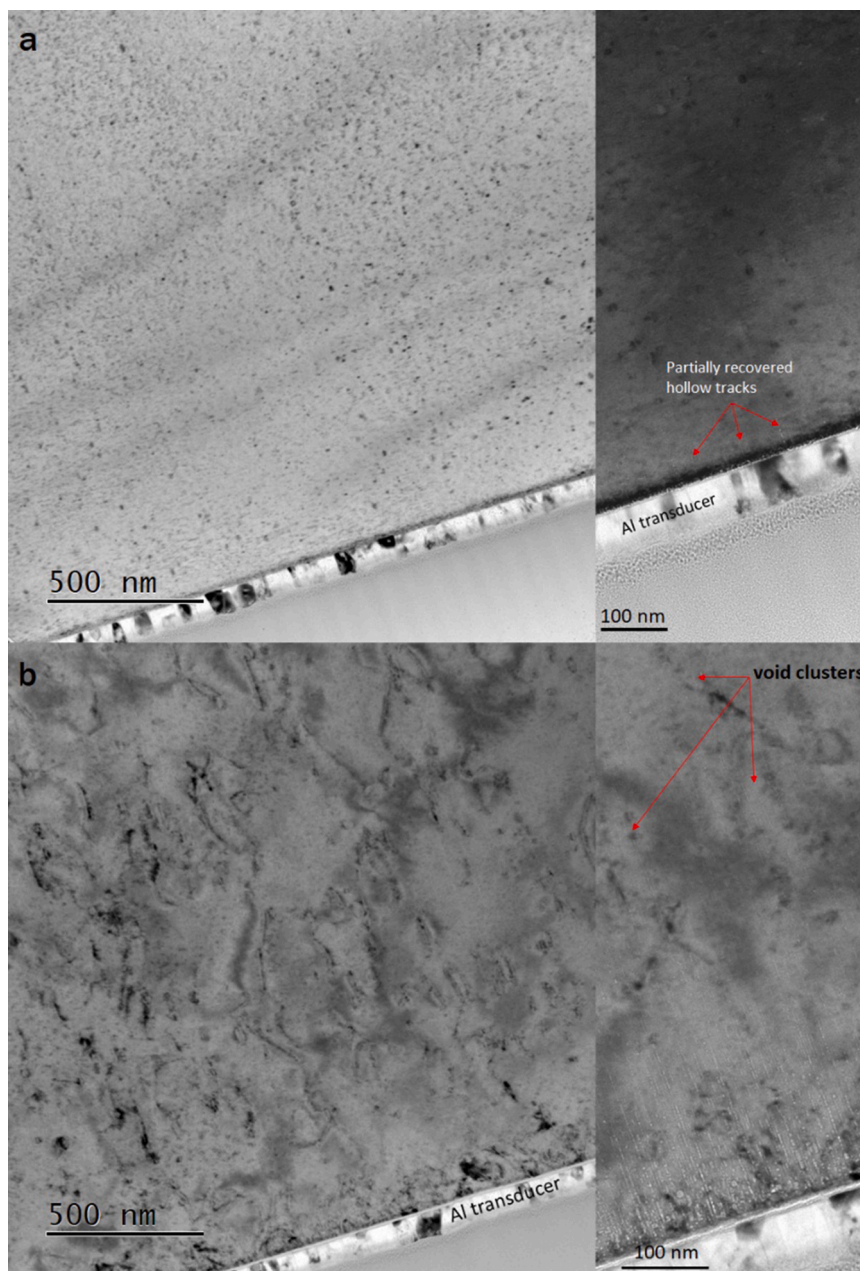
Fig. 6. (a) Bright field TEM image of 6×10^{10} ion/cm^2 irradiated ZnO after annealing. The inset shows a higher magnification underfocused image of the same region. (b) Bright field image of a 6×10^{12} ion/cm^2 irradiated ZnO after annealing. The inset shows an underfocused higher magnification image of the same region.

3.3. Simulation of k in pristine zno

To calculate the effect of SHI induced defects on k, simulations for pristine ZnO were initially performed. Fig. 8a shows the normalized autocorrelation function at room temperature as a function of correlation time. The plot exhibits an oscillatory pattern, which was previously reported for ZnO [29]. The large oscillations in the autocorrelation function made determining the thermal conductivity using the Green-Kubo relation difficult because the noise levels were too high to identify a convergence region. In order to improve the statistics, ten independent trajectories were calculated as shown in Fig. 8b, where the room-temperature k along the c-direction is given as a function of correlation time. The k_{cc} value already reached saturation at 100 ps correlation time. The estimated value of k_{cc} for the PCRIM potential was 27.2 ± 1.6 W $m^{-1} K^{-1}$. This value is approximately 30 % lower than the experimental measurements and lower than the previously reported

EMD value for Buckingham potential [29]. This discrepancy is likely due to the IAP that was used and might be attributed to the uncertainty in the EMD method itself [62]. Nevertheless, to check the reliability of these values, we also performed calculations of k_{cc} using BTE-RTA. The estimated k_{cc} value for the PCRIM potentials obtained from BTE-RTA was 31.2 W $m^{-1} K^{-1}$. The values are consistent with EMD results and earlier reported work for the Buckingham IAP [29]. We thus obtained optimal correlation and simulation times for further Green-Kubo calculations.

3.4. Simulated k of SHI irradiated ZnO

Fig. 9 shows the TREKIS simulated relaxation process of a damaged ZnO supercell at 1, 5, 30 and 100 ps after 710 MeV Bi ion passage. It shows the diamond structure identified in OVITO software using a modified version of common neighbor analysis [63]. The black dots
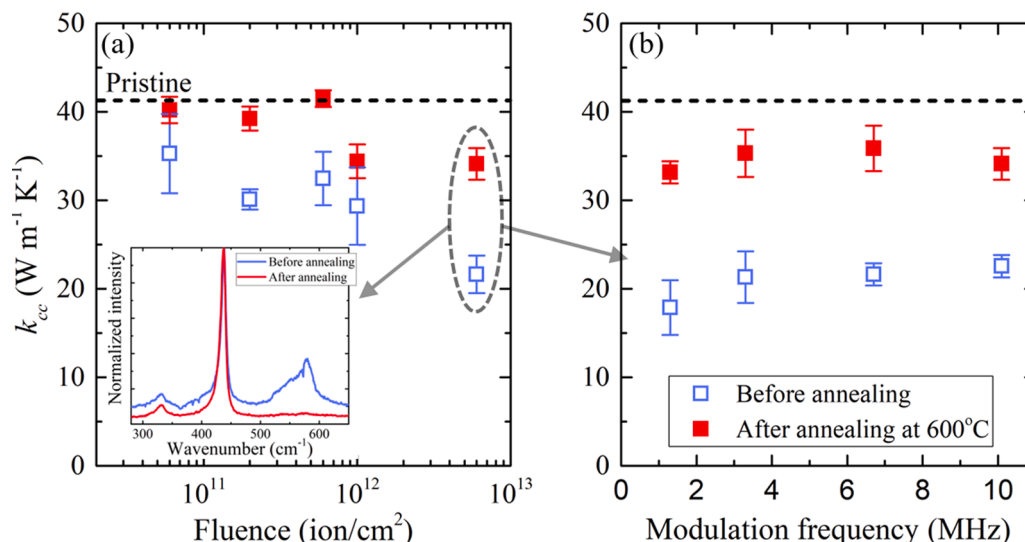
Fig. 7. (a) Thermal conductivity vs ion fluence of irradiated ZnO samples before (open squares) and after (solid squares) annealing. The inset shows the Raman spectra of the 6×10^{12} ion/cm^2 irradiated sample before and after annealing. (b) k_{cc} vs pump modulation frequency of the 6×10^{12} ion/cm^2 irradiated sample before and after annealing.
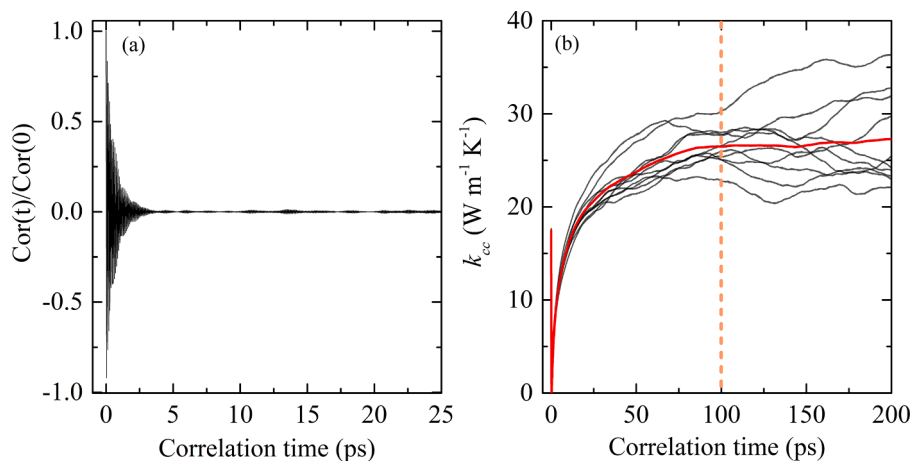

Fig. 8. (a) Correlation function dependence on correlation and simulation times from eq. (1) for the PCRIM potential. (b) k_{cc} as a function of correlation time for different trajectories of atoms for the PCRIM potential. The red line indicates the average k_{cc} value.

represent atoms displaced from their diamond crystal lattice positions while the white area indicates an undamaged ZnO lattice. At 1 ps after ion passage, a large damage area $\sim$ 5 nm in diameter was formed. This region rapidly shrunk (over $\sim$30 ps) due to recrystallization and finally formed a discontinuous ion track *containing individual vacancies and interstitials* (at 100 ps) which was validated by the above structural analysis. *The simulated structure confirmed the absence of amorphization and extended defects such as dislocations.* Simulation results showed that ion irradiation produces only point defects (vacancies and interstitials) in ZnO, which is in agreement with our Raman measurements performed in this work and TEM results shown above. It should be noted that we did not take the lattice strain into account in our simulations. The reason is two-fold: firstly, the simulations were performed under constant volume as was described in the methods section. Secondly, our measured strain values (from XRD) were too low to have an observable impact on the thermal conductivity [29]. TEM images indicated that the stress fluctuates significantly over small distances and thus quantification of the stress is not trivial and will be the subject of future investigations.

Fig. 10 shows TREKIS simulated damaged structures after relaxation to room temperature. We performed Wigner-Seitz defect analysis implemented into OVITO software to visualize point defects (Fig. 10)

and estimate their concentration [64]. This method involves comparing a disturbed crystal with a perfect, defect-free crystal, which reveals whether the initial atomic site (Wigner-Seitz cell) is occupied by the absence of an atom (vacancy) or by more than one atom (interstitial). Simulations of two sequential ions in the ZnO lattice were performed to estimate the ion interaction distance (see details in Section II, Modelling). *At ion paths separations of < 6 nm, the second ion annealed all defects produced by the first ion impact* (example of 3 nm separation is shown in Fig. 11(a) and (b)). In contrast, at 6 nm separation, the first ion-induced point defects *remain* after the second ion impact Fig. 11(c) and (d). Therefore, at separations $\leq$ 6 nm, nearest neighbor ions start to affect existing tracks.

To calculate *k* in the ion damaged region, the simulation box was cut into a $6.2 \times 6.2 \times 9.9$ nm^3 box by sustaining the lattice periodicity as shown in Fig. 10, corresponding to the calculated *threshold separation distance of 6 $\pm$ 1 nm between isolated ion tracks and, approximately, to a fluence of $\sim$ 2.6 $\pm$ 0.8 $\times$ 10^{12} ion/cm^2*. The extracted supercell was directly fed into the EMD Green-Kubo method for determination of *k*. The estimated thermal conductivity of the extracted cell for the PCRIM potential was 15.2 ± 1.1 W m^{-1} K^{-1} which is almost half of the pristine thermal conductivity determined by the Green-Kubo method.
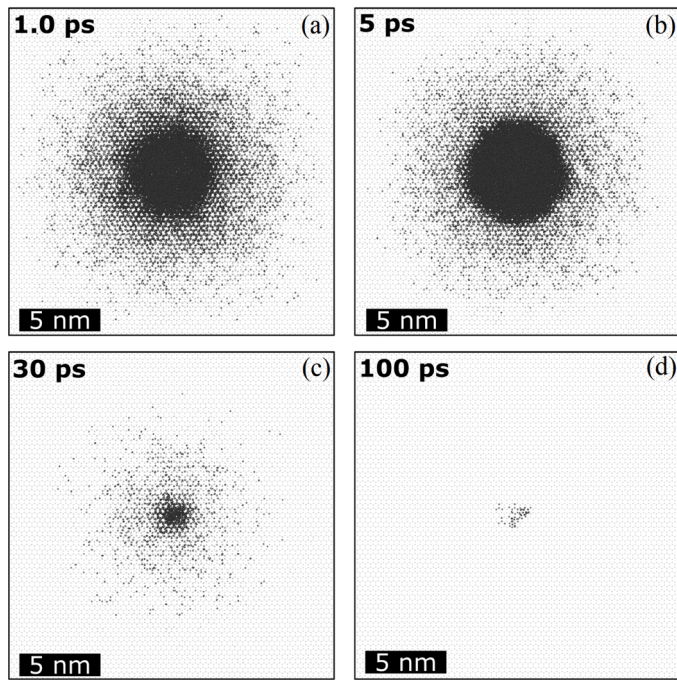
Fig. 9. Top view of different time snapshots of a ZnO supercell after 710 MeV Bi ion passage.

We also determined the effective *k* using the Rayleigh model based on an effective medium approximation [65,66]. Although this model is typically applied to spherical particles embedded in a continuous matrix [65], it was found to be compatible with ion track structures [66]. We assumed that the damaged volume created in a track is approximately cylindrical in shape. According to the Rayleigh model the effective *k* is given by [66]:

$$\kappa_{eff} = \kappa_p(1 - \sigma_d) + \kappa_d \sigma_d, \tag{7}$$

where κ_p and κ_d are conductivities of the pristine and central damaged regions, respectively. $\sigma_d = 1 - e^{-\pi r^2 \Phi}$ and *r* is the radius of the damaged region, estimated to be ~ 3 nm. This is very similar to the direct impact model mentioned previously for the Klemens model [16,17].

Fig. 12 shows the calculated thermal conductivity as a function of ion dose and ion path separation distance for simulated ZnO crystals along

with TDTR data. The k_{cc} decayed with increased ion fluence and saturated at the highest doses due to overlapping of the damaged volumes. This is in overall agreement with the trend of measured conductivities. The difference among the various models is evident. The semi-analytical Klemens model appears to align most closely with the experimental results. However, it requires accurate representation of phonons with different mean free paths. TREKIS+MD+Rayleigh k_{cc} values for the PCRIM potential shows a reasonable agreement with the experimental data. Although it underestimates the effect of SHI damage on the degradation of thermal conductivity for the normalized k_{cc}, the model still captures the effect of track overlapping at the highest doses.

It should be noted that the presented TREKIS+MD+Rayleigh model is *one of the first attempts* to simulate the thermal conductivity of SHI irradiated semiconducting solid crystals *without free parameters*. Currently, the model is oversimplified mainly due to the use of the Rayleigh model which does not fully capture the effective conductivity of nanoscale tracks, because it assumes a cylindrical shape of tracks. In reality, ion tracks in ZnO are more complicated consisting of loosely aligned point defects and small defect clusters. Another issue is related to interatomic potentials. We tried several potentials as mentioned in the text and PCRIM was found to be the most suitable in terms of stability of the final structure and computational cost. However, it might underestimate the concentration of defects and does not take into account surface damage that results from SHI irradiation such as hillock formation and the associated hollow tracks in the near surface region. Future work will be dedicated to identifying a suitable potential that can account for all these effects. IAPs play a major role in correctly predicting radiation damage-induced crystal straining and more work should be done to develop a suitable IAP using novel approaches such as machine learning methods [67].

Nevertheless, the current TREKIS+MD+Rayleigh model involving the PCRIM potential still *reproduces the transition from single impact to ion path overlapping regimes* occurring *at the threshold fluence of $\geq 2.6 \pm 0.8 \times 10^{12}$ ion/cm^2 corresponding to a critical track separation of 6 ± 1 nm.* Below this distance the thermal conductivity tends to saturate, which can be explained by the effective thermal annealing of radiation induced point defects. Such annealing is mediated by the intense heat generated from neighboring ion impact events, provided that the distance between these neighboring ion paths is below 6 nm.

4. Conclusion

In this study, we introduced a novel approach of multiscale defect characterization in SHI irradiated single crystalline ZnO. The method
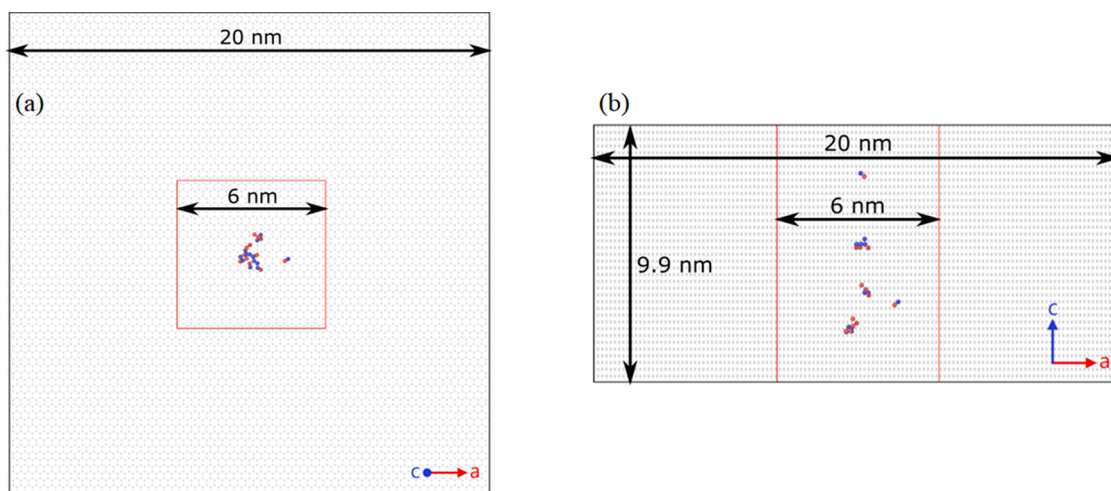

Fig. 10. Visualization of resulting lattices after TREKIS and MD simulation of a single 710 MeV Bi ion impact (a) top view, (b) side view. Red lines indicate the boundary for EMD calculations.
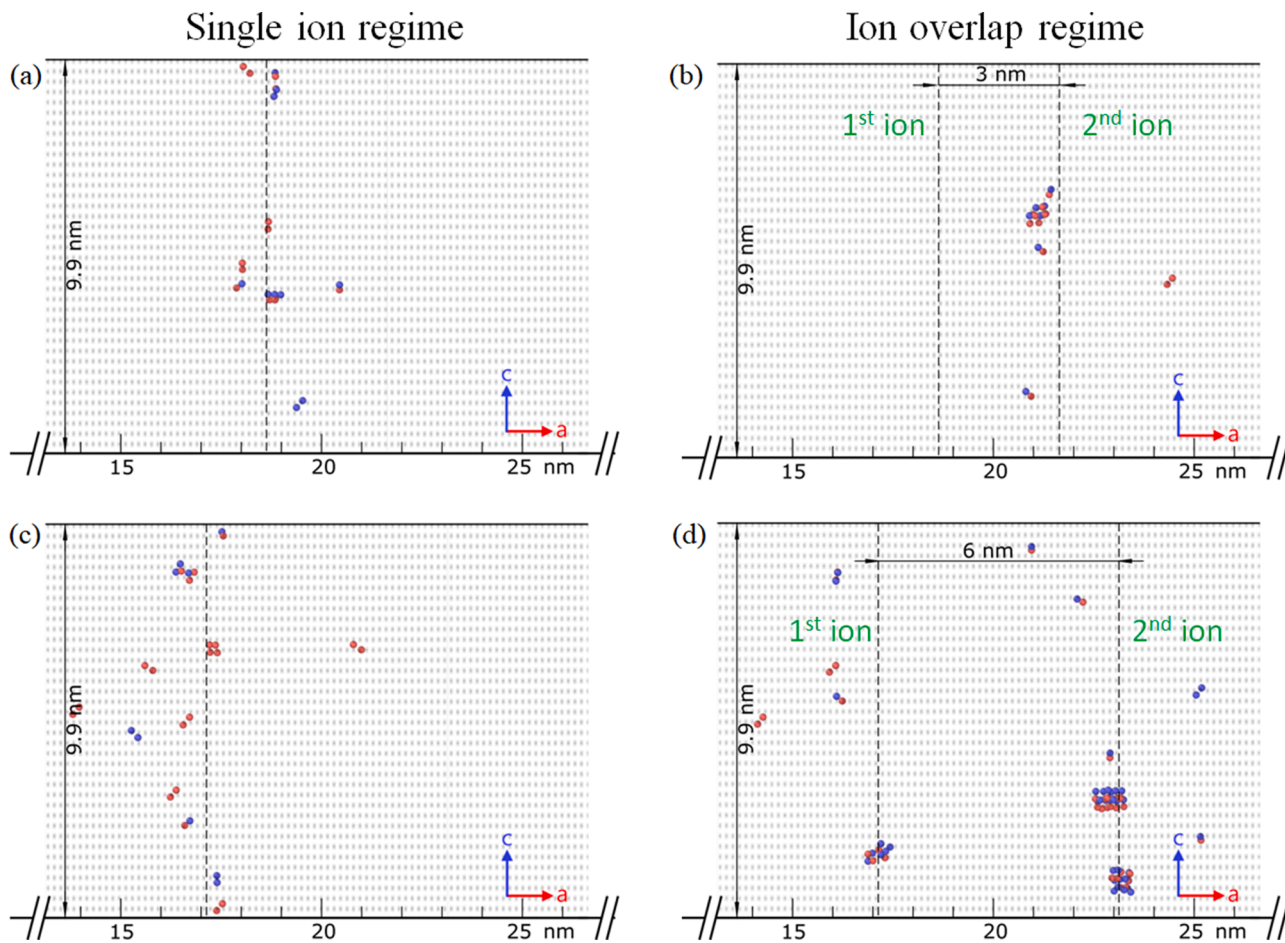
Fig. 11. Visualization of resulting lattices after TREKIS and MD simulation of two sequential 710 MeV Bi ions. (a) and (c) 1st damage, (b) 2nd ion damage at 3 nm separation, (d) 2nd ion damage at 6 nm separation. Dashed lines indicate the ion path.
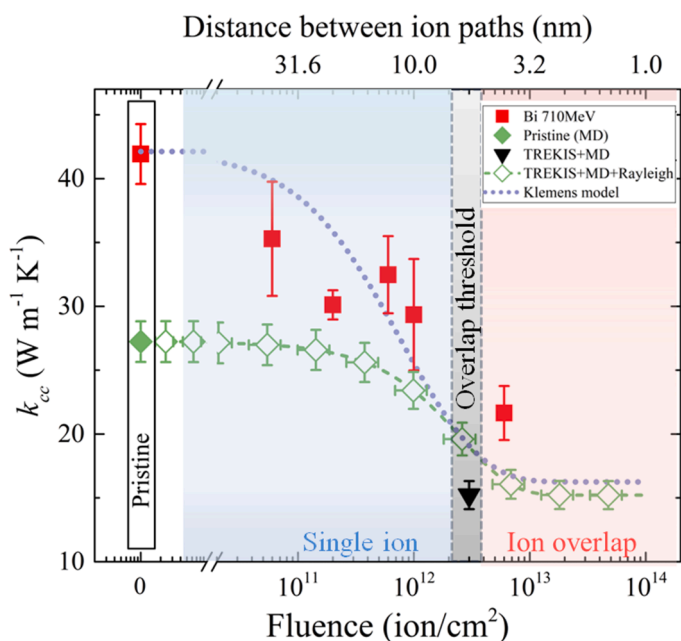

Fig. 12. Absolute values of both the experimentally measured and calculated thermal conductivity (*k*) as a function of fluence and the distance between ion paths.

encompasses nanoscale thermal conductivity (TDTR) validated by structural characterization (XRD, Raman and TEM), and a hybrid atomistic modelling technique based on TREKIS and MD with the PCRIM interatomic potential along with the Rayleigh effective medium approximation and semi-analytical Klemens phonon scattering models.

ZnO crystals were irradiated with 710 MeV Bi ions at room temperature and with fluences ranging over 10^{10}–10^{13} ion/cm^2. XRD analysis demonstrated that ZnO undergoes *radiation-induced straining and defect formation,* but *maintains its crystallinity* with no sign of amorphization, or phase transformation, which proves the *extreme radiation resistance* of this material. Raman measurements revealed that irradiation by Bi ions produce point defects in the form of oxygen vacancies and zinc interstitials which are effectively removed by annealing at 600 °C.

TEM analysis supported the XRD result regarding the presence of strain and maintained crystallinity and further showed the presence of vacancy clusters and hollow tracks as well as the formation of dislocations after irradiation at higher fluences followed by thermal annealing.

TDTR measurements demonstrated a *thermal conductivity reduction with increased ion dose in the single ion impact regime, and saturation of the thermal conductivity reduction in the ion path overlapping regime.* Quasistatic temperature annealing resulted in near complete removal of point defects, but with the start of ion path overlapping, complex clusters and extended defect formation lead to only partial recovery of *k* after annealing.

A pivotal aspect of this research was the integration of TREKIS with MD simulation to directly calculate the thermal transport change in a SHI damaged structure without adjustable parameters. The numerical

results show a fair agreement with the experiments, *clearly capturing the effect of single ion impact and ion path overlapping regimes*. Therefore, this method may provide the most accurate representation of the nanoscale evolution of point defects during SHI bombardment. It elucidates their eventual effect on *thermal transport degradation at low doses and saturation at high doses due to mutual thermal annealing of radiation defects. This annealing occurs by ion induced events taking place in the nanometer-scale vicinity of ion trajectories*.

CRediT authorship contribution statement

Azat Abdullaev: Writing – original draft, Visualization, Validation, Methodology, Investigation, Formal analysis, Data curation, Conceptualization. **Kairolla Sekerbayev:** Writing – review & editing, Validation, Software, Investigation, Formal analysis. **Ruslan Rymzhanov:** Software, Methodology, Investigation. **Vladimir Skuratov:** Resources, Investigation. **Jacques O Connell:** Writing – review & editing, Visualization, Validation, Investigation, Formal analysis. **Bekdaulet Shukirgaliyev:** Resources, Investigation. **Artem Kozlovskiy:** Validation, Investigation, Formal analysis, Data curation. **Yanwei Wang:** Writing – review & editing, Software, Investigation. **Zhandos Utegulov:** Writing – review & editing, Supervision, Resources, Investigation, Funding acquisition.

Declaration of competing interest

The authors declare that they have no known competing financial interests or personal relationships that could have appeared to influence the work reported in this paper.

Data availability

Data will be made available on request.

Supplementary materials

Supplementary material associated with this article can be found, in the online version, at doi:10.1016/j.materresbull.2024.112786.

References

[1] A. Giri, A.Z. Chen, A. Mattoni, K. Aryana, D. Zhang, X. Hu, S.H. Lee, J.J. Choi, P. E. Hopkins, Ultralow thermal conductivity of two-dimensional metal halide perovskites, Nano Lett. (2020) 20, https://doi.org/10.1021/acs.nanolett.0c00214.

[2] K. Chen, B. Song, N.K. Ravichandran, Q. Zheng, X. Chen, H. Lee, H. Sun, S. Li, G.A. G.U. Gamage, F. Tian, et al., Ultrahigh thermal conductivity in isotope-enriched cubic boron nitride, Science (1979) (2020) 367, https://doi.org/10.1126/science. aaz6149.

[3] A. Giri, P.E. Hopkins, A review of experimental and computational advances in thermal boundary conductance and nanoscale thermal transport across solid interfaces, Adv. Funct. Mater. (2020) 30.

[4] Y.K. Koh, Y. Cao, D.G. Cahill, D. Jena, Heat-transport mechanisms in superlattices, Adv. Funct. Mater. 19 (2009) 610–615, https://doi.org/10.1002/adfm.200800984.

[5] M.N. Luckyanova, J. Garg, K. Esfarjani, A. Jandl, M.T. Bulsara, A.J. Schmidt, A. J. Minnich, S. Chen, M.S. Dresselhaus, Z. Ren, et al., Coherent phonon heat conduction in superlattices, Science (1979) (2012) 338, https://doi.org/10.1126/science.1225549.

[6] C.S. Gorham, K. Hattar, R. Cheaito, J.C. Duda, J.T. Gaskins, T.E. Beechem, J. F. Ihlefeld, L.B. Biedermann, E.S. Piekos, D.L. Medlin, et al., Ion irradiation of the native oxide/silicon surface increases the thermal boundary conductance across aluminum/silicon interfaces, Phys. Rev. B Condens. Matter. Mater. Phys. (2014) 90, https://doi.org/10.1103/PhysRevB.90.024301.

[7] Y. Zhao, D. Liu, J. Chen, L. Zhu, A. Belianinov, O.S. Ovchinnikova, R.R. Unocic, M. J. Burch, S. Kim, H. Hao, et al., Engineering the thermal conductivity along an individual silicon nanowire by selective helium ion irradiation, Nat. Commun. 8 (2017), https://doi.org/10.1038/ncomms15919.

[8] N. Tureson, M. Marteau, T. Cabioch, N. van Nong, J. Jensen, J. Lu, G. Greczynski, D. Fournier, N. Singh, A. Soni, et al., Effect of ion-implantation-induced defects and mg dopants on the thermoelectric properties of ScN, Phys. Rev. B (2018) 98, https://doi.org/10.1103/PhysRevB.98.205307.

[9] S. Alaie, M.G. Baboly, Y.B. Jiang, S. Rempe, D.H. Anjum, S. Chaieb, B.F. Donovan, A. Giri, C.J. Szwejkowski, J.T. Gaskins, et al., Reduction and increase in thermal conductivity of si irradiated with Ga+ via focused ion beam, ACS. Appl. Mater. Interfaces. (2018) 10, https://doi.org/10.1021/acsami.8b11949.

[10] E.A. Scott, S.W. King, N.N. Jarenwattananon, W.A. Lanford, H. Li, J. Rhodes, P. E. Hopkins, Thermal conductivity enhancement in ion-irradiated hydrogenated amorphous carbon films, Nano Lett. 21 (2021), https://doi.org/10.1021/acs. nanolett.1c00616.

[11] R. Neumann, Science and technology on the nanoscale with swift heavy ions in matter, Nucl. Instrum. Methods Phys. Res. B 314 (2013) 4–10, https://doi.org/10.1016/j.nimb.2013.04.035.

[12] F.F. Komarov, Nano- and microstructuring of solids by swift heavy ions, Uspekhi Fizicheskih Nauk 187 (2017) 465–504, https://doi.org/10.3367/ufnr.2016.10.038012.

[13] M. Lang, F. Djurabekova, N. Medvedev, M. Toulemonde, C. Trautmann, Fundamental phenomena and applications of swift heavy ion irradiations. Comprehensive Nuclear Materials: Second Edition, 2020.

[14] F. Aumayr, S. Facsko, A.S. El-Said, C. Trautmann, M. Schleberger, Single Ion Induced Surface Nanostructures: a Comparison between Slow Highly Charged and Swift Heavy Ions, J. Phys. Condens. Matter (2011).

[15] J.H. O'Connell, G. Aralbayeva, V.A. Skuratov, M. Saifulin, A. Janse Van Vuuren, A. Akilbekov, M. Zdorovets, Temperature dependence of swift heavy ion irradiation induced hillocks in TiO2, Mater. Res. Express. 5 (2018), https://doi.org/10.1088/2053-1591/aac0ce.

[16] A. Abdullaev, A. Koshkinbayeva, V. Chauhan, Z. Nurekeyev, J. O'Connell, A.J. van Vuuren, V. Skuratov, M. Khafizov, Z.N. Utegulov, Depth-resolved thermal conductivity and damage in swift heavy ion irradiated metal oxides, J. Nucl. Mater. (2022) 561, https://doi.org/10.1016/j.jnucmat.2022.153563.

[17] A. Abdullaev, V.S. Chauhan, B. Muminov, J. O'Connell, V.A. Skuratov, M. Khafizov, Z.N. Utegulov, Thermal transport across nanoscale damage profile in sapphire irradiated by swift heavy ions, J. Appl. Phys. (2020) 127, https://doi.org/10.1063/1.5126413.

[18] A. Koshkinbayeva, A. Abdullaev, Z. Nurekeyev, V.A. Skuratov, Y. Wang, M. Khafizov, Z. Utegulov, Thermal transport and optical spectroscopy in 710-MeV Bi Ion irradiated LiF crystals, Nucl. Instrum. Methods Phys. Res. B 475 (2020) 14–19, https://doi.org/10.1016/j.nimb.2020.04.006.

[19] V.S. Chauhan, A. Abdullaev, Z. Utegulov, J. O'Connell, V. Skuratov, M. Khafizov, Simultaneous characterization of cross- and in-plane thermal transport in insulator patterned by directionally aligned nano-channels, AIP Adv. 10 (2020), https://doi.org/10.1063/1.5125415.

[20] A.Y. Azarov, A.I. Titov, P.A. Karaseov, S.O. Kucheyev, A. Hallén, A.Y. Kuznetsov, B. G. Svensson, A.P. Pathak, Structural damage in ZnO bombarded by heavy ions, Vacuum. (2010) 84, https://doi.org/10.1016/j.vacuum.2009.10.041.

[21] S.O. Kucheyev, J.S. Williams, C. Jagadish, J. Zou, C. Evans, A.J. Nelson, A. v. Hamza, Ion-beam-produced structural defects in ZnO, Phys. Rev. B Condens. Matter. Mater. Phys. 67 (2003), https://doi.org/10.1103/PhysRevB.67.094115.

[22] O.H. Pakarinen, F. Djurabekova, K. Nordlund, Density evolution in formation of swift heavy ion tracks in insulators, in: Proceedings of the Nuclear Instruments and Methods in Physics Research, Section B: Beam Interactions with Materials and Atoms 268, 2010.

[23] M. Toulemonde, C. Dufour, E. Paumier, Transient thermal process after a high-energy heavy-ion irradiation of amorphous metals and semiconductors, Phys. Rev. B (1992) 46, https://doi.org/10.1103/PhysRevB.46.14362.

[24] A. Meftah, F. Brisard, J.M. Costantini, E. Dooryhee, M. Hage-Ali, M. Hervieu, J. P. Stoquert, F. Studer, M. Toulemonde, Track formation in SiO2 quartz and the thermal-spike mechanism, Phys. Rev. B 49 (1994) 12457–12463, https://doi.org/10.1103/PhysRevB.49.12457.

[25] C. Dufour, M. Toulemonde, Models for the description of track formation. Springer Series in Surface Sciences, 2016, p. 61.

[26] T. Tsubota, M. Ohtaki, K. Eguchi, H. Arai, Thermoelectric properties of Al-doped ZnO as a promising oxide material for high-temperature thermoelectric conversion, J. Mater. Chem. 7 (1997), https://doi.org/10.1039/a602506d.

[27] M. Ohtaki, K. Araki, K. Yamamoto, High thermoelectric performance of dually doped ZnO ceramics, Proc. J. Electron. Mater. 38 (2009).

[28] P. Jood, R.J. Mehta, Y. Zhang, G. Peleckis, X. Wang, R.W. Siegel, T. Borca-Tasciuc, S.X. Dou, G. Ramanath, Al-doped Zinc oxide nanocomposites with enhanced thermoelectric properties, Nano Lett. (2011) 11, https://doi.org/10.1021/nl202439h.

[29] J.A. Seijas-Bellido, R. Rurali, J. Íñiguez, L. Colombo, C. Melis, Strain engineering of ZnO thermal conductivity, Phys. Rev. Mater. 3 (2019), https://doi.org/10.1103/PhysRevMaterials.3.065401.

[30] J.F. Ziegler, M.D. Ziegler, J.P. Biersack, SRIM - the stopping and range of ions in matter (2010), Nucl. Instrum. Methods Phys. Res. B 268 (2010) 1818–1823, https://doi.org/10.1016/j.nimb.2010.02.091.

[31] P. Jiang, X. Qian, R.Tutorial Yang, Time-domain Thermoreflectance (TDTR) for thermal property characterization of bulk and thin film materials, J. Appl. Phys. (2018) 124.

[32] D.G. Cahill, Analysis of heat flow in layered structures for time-domain Thermoreflectance, Rev. Sci. Instrum. (2004), https://doi.org/10.1063/1.1819431.

[33] R.A. Rymzhanov, N. Medvedev, J.H. O'Connell, V.A. Skuratov, A. Janse van Vuuren, S.A. Gorbunov, A.E. Volkov, Insights into different stages of formation of swift heavy ion tracks, Nucl. Instrum. Methods Phys. Res. B (2020) 473, https://doi.org/10.1016/j.nimb.2020.04.005.

[34] N.A. Medvedev, R.A. Rymzhanov, A.E. Volkov, Time-resolved electron kinetics in swift heavy ion irradiated solids, J. Phys. D. Appl. Phys. (2015) 48, https://doi.org/10.1088/0022-3727/48/35/355303.

[35] R.A. Rymzhanov, N.A. Medvedev, A.E. Volkov, Effects of model approximations for electron, hole, and photon transport in swift heavy ion tracks, Nucl. Instrum. Methods Phys. Res. B (2016) 388, https://doi.org/10.1016/j.nimb.2016.11.002.

[36] A.P. Thompson, H.M. Aktulga, R. Berger, D.S. Bolintineanu, W.M. Brown, P. S. Crozier, P.J. t Veld, A. Kohlmeyer, S.G. Moore, T.D. Nguyen, et al., LAMMPS - a flexible simulation tool for particle-based materials modeling at the atomic, meso, and continuum scales, Comput. Phys. Commun. (2022) 271, https://doi.org/10.1016/j.cpc.2021.108171.

[37] R.A. Voronkov, R.A. Rymzhanov, N.A. Medvedev, A.E. Volkov, Monte-carlo modeling of excitation of the electron subsystem of ZnO and MgO in tracks of swift heavy ions, Nucl. Instrum. Methods Phys. Res. B (2015) 365, https://doi.org/10.1016/j.nimb.2015.07.088.

[38] Barkas Walter H. *Nuclear Research Emulsions*; New-York, 1963.

[39] H.J.C. Berendsen, J.P.M. Postma, W.F. van Gunsteren, A. DiNola, J.R. Haak, Molecular dynamics with coupling to an external bath, J. Chem. Phys. 81 (1984) 3684–3690, https://doi.org/10.1063/1.448118.

[40] A. Stukowski, Visualization and analysis of atomistic simulation data with OVITO–the open visualization tool, Model. Simul. Mat. Sci. Eng. 18 (2010) 015012, https://doi.org/10.1088/0965-0393/18/1/015012.

[41] P. Erhart, N. Juslin, O. Goy, K. Nordlund, R. Müller, K. Albe, Analytic bond-order potential for atomistic simulations of Zinc oxide, J. Phys. Condens. Matter 18 (2006), https://doi.org/10.1088/0953-8984/18/29/003.

[42] D. Raymand, A.C.T. van Duin, M. Baudin, K. Hermansson, A reactive force field (ReaxFF) for Zinc oxide, Surf. Sci. (2008) 602, https://doi.org/10.1016/j.susc.2007.12.023.

[43] S. Wang, Z. Fan, R.S. Koster, C. Fang, M.A. van Huis, A.O. Yalcin, F.D. Tichelaar, H. W. Zandbergen, T.J.H. Vlugt, New Ab initio based pair potential for accurate simulation of phase transitions in ZnO, J. Phys. Chem. C 118 (2014) 11050–11061, https://doi.org/10.1021/jp411308z.

[44] M. Nyberg, M.A. Nygren, L.G.M. Pettersson, D.H. Gay, A.L. Rohl, Hydrogen dissociation on reconstructed ZnO surfaces, J. Phys. Chem. 100 (1996) 9054–9063, https://doi.org/10.1021/jp953704h.

[45] A. Roy, Y.T. Cheng, M.L. Falk, Amorphous ZnO-based compounds as thermoelectrics, J. Phys. Chem. C (2016) 120, https://doi.org/10.1021/acs.jpcc.5b11618.

[46] H.T. Wu, Y.C. Su, C.W. Pao, C.F. Shih, ZnO/Silicon-rich oxide superlattices with high thermoelectric figure of merit: a comprehensive study by experiment and molecular dynamic simulation, ACS. Appl. Mater. Interfaces. (2019) 11, https://doi.org/10.1021/acsami.8b20725.

[47] R. Kubo, M. Yokota, S. Nakajima, Statistical-mechanical theory of irreversible processes. II. Response to thermal disturbance, J. Phys. Soc. Jpn. 12 (1957) 1203–1211, https://doi.org/10.1143/JPSJ.12.1203.

[48] M.S.Markoff Green, Random processes and the statistical mechanics of time-dependent phenomena. II. Irreversible processes in fluids, J. Chem. Phys. 22 (1954) 398–413, https://doi.org/10.1063/1.1740082.

[49] R.W. Hockney, J.W. Eastwood, The particle-mesh force calculation, Comput. Simul Using Part. Adam. Hilger Bristol. New York NY, USA (1989) 120–165.

[50] A. Neelov, C. Holm, Interlaced P3M algorithm with analytical and IK-differentiation, J. Chem. Phys. 132 (2010) 234103, https://doi.org/10.1063/1.3430521.

[51] T. Tadano, Y. Gohda, S. Tsuneyuki, Anharmonic force constants extracted from first-principles molecular dynamics: applications to heat transfer simulations, J. Phys. Condens. Matter 26 (2014) 225402, https://doi.org/10.1088/0953-8984/26/22/225402.

[52] P.G. Klemens, Theory of thermal conduction in dielectric solids: effects of radiation damage, Nucl. Inst. Methods Phys. Res B 1 (1984) 204–208, https://doi.org/10.1016/0168-583X(84)90070-3.

[53] V.A. Skuratov, N.S. Kirilkin, Y.S. Kovalev, T.S. Strukova, K. Havanscak, Depth-Resolved Photo- and Ionoluminescence of LiF and Al 2O 3, in: Proceedings of the Nuclear Instruments and Methods in Physics Research, Section B: Beam Interactions with Materials and Atoms 286, 2012, pp. 61–66, https://doi.org/10.1016/j.nimb.2011.12.037.

[54] G. Sattonnay, S. Moll, M. Herbst-Ghysel, C. Legros, J.M. Costantini, L. Thomé, Mechanical stresses induced in ceramic oxides by ion irradiation, Nucl. Instrum. Methods Phys. Res. B (2008) 266, https://doi.org/10.1016/j.nimb.2008.03.162.

[55] G. Sattonnay, M. Lahrichi, M. Herbst-Ghysel, F. Garrido, L. Thoń, Stress field induced by swift heavy ion irradiation in cubic yttria stabilized zirconia, J. Appl. Phys. 101 (2007), https://doi.org/10.1063/1.2733745.

[56] G. Sattonnay, M. Lahrichi, A. Benyagoub, J.M. Costantini, F. Garrido, L. Thomé, C. Trautmann, Structural modifications induced by swift heavy ions in cubic stabilized zirconia: an X-Ray diffraction investigation, Nucl. Instrum. Methods Phys. Res. B (2007) 257, https://doi.org/10.1016/j.nimb.2007.01.238.

[57] Z.Q. Chen, A. Kawasuso, Y. Xu, H. Naramoto, X.L. Yuan, T. Sekiguchi, R. Suzuki, T. Ohdaira, Production and recovery of defects in phosphorus-implanted ZnO, J. Appl. Phys. (2005) 97, https://doi.org/10.1063/1.1821636.

[58] Y. Song, S. Zhang, C. Zhang, Y. Yang, K. Lv, Raman Spectra and microstructure of zinc oxide irradiated with swift heavy ion, Crystals (Basel) 9 (2019), https://doi.org/10.3390/cryst9080395.

[59] A. Jagerová, R. Mikšová, O. Romanenko, I. Plutnarova, Z. Sofer, P. Slepička, J. Mistrík, A. Macková, Surface modification by high-energy heavy-ion irradiation in various crystalline ZnO facets, Phys. Chem. Chem. Phys. 23 (2021) 22673–22684, https://doi.org/10.1039/d1cp02388h.

[60] X. Wu, J. Lee, V. Varshney, J.L. Wohlwend, A.K. Roy, T. Luo, Thermal conductivity of wurtzite zinc-oxide from first-principles lattice dynamics - A comparative study with gallium nitride, Sci. Rep. 6 (2016), https://doi.org/10.1038/srep22504.

[61] G. Perillat-Merceroz, P. Gergaud, P. Marotel, S. Brochen, P.-H. Jouneau, G. Feuillet, S. Brochen, Formation and annealing of dislocation loops induced by nitrogen implantation of ZnO, J. Appl. Phys. 109 (2011) 23513, https://doi.org/10.1063/1.3537917i.

[62] A.J.H. McGaughey, M. Kaviany, Thermal conductivity decomposition and analysis using molecular dynamics simulations. Part I. Lennard-Jones Argon, Int. J. Heat. Mass Transf. (2004) 47, https://doi.org/10.1016/j.ijheatmasstransfer.2003.11.002.

[63] E. Maras, O. Trushin, A. Stukowski, T. Ala-Nissila, H. Jónsson, Global transition path search for dislocation formation in Ge on Si(001), Comput. Phys. Commun. (2016) 205, https://doi.org/10.1016/j.cpc.2016.04.001.

[64] A. Stukowski, Structure identification methods for atomistic simulations of crystalline materials, Model. Simul. Mat. Sci. Eng. 20 (2012), https://doi.org/10.1088/0965-0393/20/4/045021.

[65] K. Pietrak, T.S. Wiśniewski, A review of models for effective thermal conductivity of composite materials, J. Pow. Technol. (2015) 95.

[66] R.A. Rymzhanov, A. Akzhunussov, A.E. Volkov, A.D. Ibrayeva, V.A. Skuratov, Thermal conductivity of Al2O3 irradiated with swift heavy ions, Nucl. Mater. Energy (2022) 33, https://doi.org/10.1016/j.nme.2022.101267.

[67] J.Perspective Behler, Machine learning potentials for atomistic simulations, J. Chem. Phys. (2016) 145, https://doi.org/10.1063/1.4966192.